doi:10.26443/seismica.v5i1.2179

Relaxing the Separation Between On-Fault and Off-Fault Seismicity Using an Empirical M_w–Deformed Area Relation

Alessandro Valentini * [1]

[1]Department of Geology, University of Vienna, Vienna, Austria

Author contributions: *Conceptualization*: Alessandro Valentini. *Funding Acquisition*: Alessandro Valentini. *Methodology*: Alessandro Valentini. *Visualization*: Alessandro Valentini. *Writing – original draft*: Alessandro Valentini.

Abstract Integrating fault-based and distributed seismicity in earthquake rupture forecasts (ERFs) is one of the challenges in probabilistic seismic hazard analysis. Traditional approaches impose a sharp distinction between on-fault and off-fault earthquakes, even though real seismicity systematically violates this separation. Moreover, combining fault and distributed sources often introduces double counting in the overlapping magnitude range and produces discontinuities in spatial earthquake rates. Here we propose a physically motivated method to relax the boundary between fault and off-fault seismicity by exploiting an empirical relation between moment magnitude (M_w) and the areal extent of permanent ground deformation derived from interferometric synthetic aperture radar observations. Using a published global dataset of 96 earthquakes, we recompute log-linear regressions between M_w and deformed area for different faulting styles and use the resulting footprint as a deformation-based buffer around each modeled seismogenic structure. Within this buffer, distributed seismicity rates for magnitudes above the minimum magnitude of the fault source are reduced using a distance-dependent power-law taper and removed entirely for points lying within the surface projection of the fault. The method produces a smooth, physically interpretable transition between fault and off-fault activity, avoids double counting, and naturally accounts for overlapping influence zones of nearby faults. This deformation-based taper provides a reproducible and easily implementable framework for improving ERFs in regions where both fault sources and distributed seismicity contribute to the overall hazard.

Production Editor: Yen Joe Tan
Handling Editor: Giuseppe Petrillo
Copy & Layout Editor: Kirsty Bayliss

Signed reviewer(s): Francesco Visini and Aybars Gürpinar

Received: December 2, 2025
Accepted: March 8, 2026
Published: April 24, 2026

1 Introduction

Probabilistic seismic hazard assessment (PSHA) offers insight into the likelihood of ground motion parameters surpassing predetermined thresholds over a specified time period at a given location (Cornell, 1968; McGuire, 1995). The two key components of PSHA are the Earthquake Rupture Forecast (ERF) and the Ground Motion Model (GMM). The ERF provides the likelihood of various fault rupture events in a region and over a specified timeframe, while the GMM quantifies ground motion shaking at specific locations following an earthquake rupture.

While traditional area-source or zonation models rely primarily on historical and/or instrumental catalogs, fault-based ERFs exploit geological and geodetic information to model rupture on mapped active and capable faults, i.e., tectonic structures that have moved in the recent geologic past, are expected to move within a future time span, and have a significant potential for displacement at or near the ground surface (International Atomic Energy Agency, 2015, 2022). A fault-based ERF captures the occurrence of large-magnitude events that may not be well represented in historical catalogs and generally produces more realistic spatial patterns of hazard. Fault-based ERFs are now standard in high-strain regions as evidenced by studies in California (Field et al., 2014) and recent seismic hazard national models for the United States (Petersen et al., 2024) and New Zealand (Gerstenberger et al., 2023), and increasingly adopted in moderate-to-low strain settings, including SE Spain (Gómez-Novell et al., 2020) and Italy (Meletti et al., 2021).

Many earthquakes in historical and instrumental catalogs, especially moment magnitude (M_w) < 5.5 events, cannot be associated unambiguously with mapped active and capable faults. Reasons for this lack of correlation include interseismic strain accumulation in areas between major faults, earthquakes occurring on unknown or blind faults, those on unmapped faults with lower slip rates, and the absence of surface ruptures associated with faults generating earthquakes below a certain magnitude threshold (typically M_w < 5.5). In such cases, seismicity is commonly referred to as diffuse seismicity—also termed off-fault, distributed, gridded, or smoothed seismicity—i.e., events that are not obviously associated with known seismogenic structures (or sources) (International Atomic Energy Agency, 2022). Nevertheless, the explicit integration of off-fault seismicity into fault-based ERF models remains essential for a comprehensive representation of seismic hazard.

*Corresponding author: alessandro.valentini@univie.ac.at

Classical approaches address this with off-fault seismicity rates for small-to-moderate magnitudes (typically between M_w 4.0 and 5.0), excluding events attributed to known seismogenic structures (i.e., on-fault seismicity) in order to avoid double counting. A combined ERF therefore merges on-fault and off-fault seismicity, but this raises a persistent challenge: ensuring a physically consistent transition between the two without introducing artificial magnitude-frequency distribution (MFD) bulges or over-forecasting.

Previous approaches include distance-based truncation, polygonal tapers, and slip-rate-based weighting functions. While effective, these methods rely on assumptions about the spatial influence of faults rather than direct observational constraints. Valentini et al. (2017) introduced a slip-rate and distance-dependent linear weighting function to combine on- and off-fault seismicity inputs. This function is applicable in the magnitude range overlapping the MFD of each seismogenic source, such that the contribution from the distributed sources linearly decreases from 1 to 0 with decreasing distance from the seismogenic source. The authors assume that in the buffer zone around the source no more than one single major fault is likely, and the buffer zone size is assumed to be controlled by the slip rate of the seismogenic source. The distance d between the fault trace of the seismogenic source and the edge of the buffer is equal to $L/2$ (L is the fault length along the strike) for sources with slip rates ≥ 1.0 mm/yr, $L/3$ for sources with slip rates of 0.3–1 mm/yr, and $L/4$ for sources with slip rates ≤ 0.3 mm/yr. The rationale behind varying distance d is given by a simple assumption: the higher the slip rate is, the larger the deformation field and the higher the value of d. Moreover, the authors assumed that given a known major seismogenic source geometrically capable of hosting a $M_w \geq 5.5$ earthquake, the possibility that a future $M_w \geq 5.5$ earthquake will occur in the vicinity of the fault, but is not caused by that source, should decrease as the distance from the seismogenic source decreases. Conversely, earthquakes with magnitudes lower than 5.5 and those due to slip along secondary faults are likely to occur everywhere within a fault system, including in proximity to the main seismogenic source. This assumption is corroborated by numerical and analogue modelling of fault system evolution (e.g., Cowie et al., 1993), which indicate the areas around major faults where it is unlikely that other major faults develop. In conclusion, depending on the positions of off-fault seismicity points with respect to the buffer zones around seismogenic sources, the rates of expected off-fault seismicity remain unmodified or decrease and can even reach zero.

Other works, such as the national seismic hazard model of New Zealand (Stirling et al., 2002, 2012), have done an additive combination of the off-fault seismicity model with the fault-based model. This creates the possibility that the same earthquake is forecast in both models, creating a potentially conservative hazard estimate, which may be seen in a bulge in the MFD in the magnitude range that overlaps between the on-fault and off-fault seismicity model. To handle this potential over-forecast, other models, such as UCERF3 (Field et al., 2014) and the new national seismic hazard model of New Zealand (Gerstenberger et al., 2023), truncated the off-fault seismicity rates at the minimum fault magnitude in regions near active faults. This is typically applied within 12 km of the fault trace (although this buffer was also dip dependent in UCERF3). The assumption is that the active fault represents a proxy for all supra-seismogenic magnitudes in that zone, and that off-fault seismicity contributes no such events in this area. To produce a smoother transition between on-fault and off-fault seismicity, Gerstenberger et al. (2023) assume that fault nucleation rates decay linearly with distance out to some specified maximum distance (12 km), and that off-fault seismicity rates have the opposite linear trend near seismogenic sources. This means that large, off-fault seismicity events can occur within 12 km of a seismogenic source, but with reduced rates that trend linearly toward zero at the fault surface. More in detail, both Field et al. (2014) and Gerstenberger et al. (2023) apply a spatially tapered weighting function to the off-fault seismicity model within the fault polygons. The function weights the off-fault model 100% at the boundaries of the polygon and uses a power-law taper to 0 at the fault location, with the fault model down-weighted to accommodate the weighting applied to the off-fault model.

In this work, we propose a new physically grounded method for combining on-fault and off-fault (i.e., diffuse) seismicity. Leveraging recent global datasets of Interferometric Synthetic Aperture Radar (InSAR) deformation, we use empirical regressions between M_w and the areal footprint of permanent ground deformation to define a deformation-based transition zone around active and capable faults. This allows us to: (1) introduce a physically constrained buffer region, (2) reduce double counting in the magnitude range of overlap, and (3) achieve a smoother and more realistic transition between on-fault and off-fault seismicity.

2 Empirical regression of dimension of deformed area and M_w

The availability of systematic global databases of surface-rupturing earthquakes has enabled the development of robust empirical relations linking earthquake size, typically expressed as moment magnitude, to the geometric dimensions of the corresponding seismogenic structures, including rupture length, rupture area, and maximum displacement (e.g., Wells and Coppersmith, 1994; Leonard, 2010; Thingbaijam et al., 2017). Advancements in remote sensing, particularly radar interferometry such as InSAR, differential high-resolution topography, and optical imagery correlation, have greatly improved our ability to detect and quantify earthquake-related ground deformation. InSAR, in particular, allows the measurement of permanent surface deformation with centimetric accuracy over regions spanning hundreds to thousands of square kilometers (Figure 1). Recent studies, such as those by Livio et al. (2017), Gürpinar et al. (2017), and Serva et al. (2019, 2025), have demonstrated a strong correlation between

M_w and the areal extent of coseismic deformation imaged through InSAR.

Livio and Ferrario (2024) compiled a global dataset of 96 earthquakes for which both M_w and the extent of the deformed area were available from InSAR observations. For each event, the authors delineated the regions of coherent deformation in both the hanging wall and footwall sides of the main fault, tracing the outermost continuous interferometric fringes. Where the location of the outermost fringe was uncertain due to incoherent or noisy signals, the mapped area was averaged, and an envelope polygon was adopted to capture the full plausible deformation footprint.

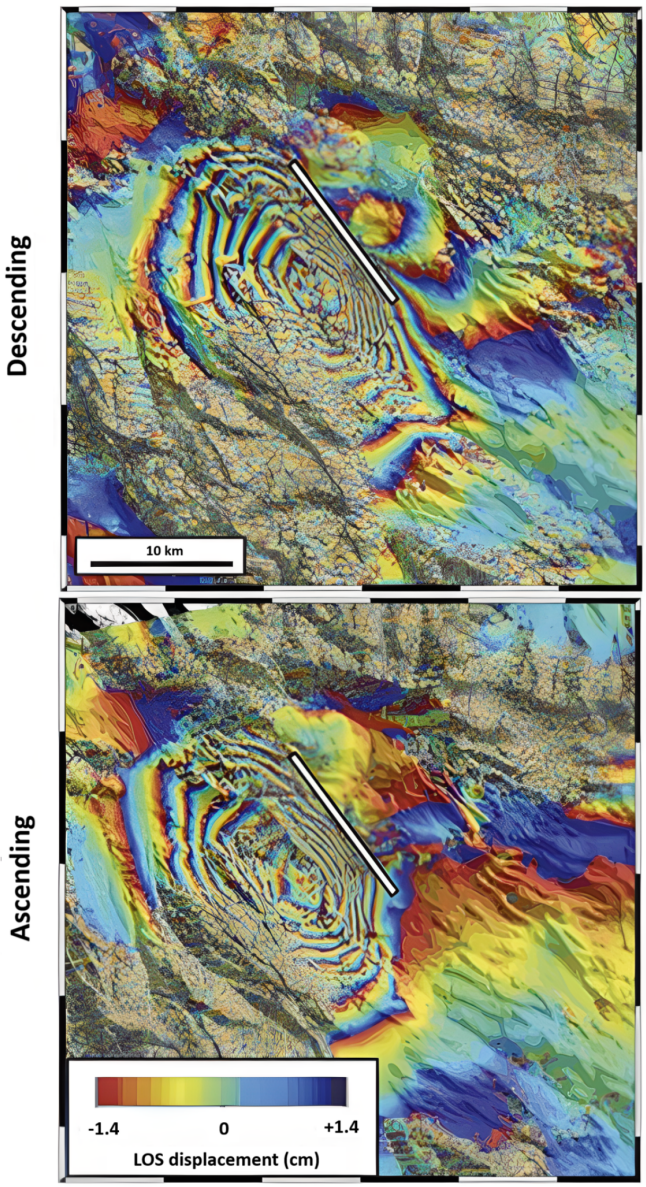

Figure 1 Data interferograms for the 2009 L'Aquila earthquake. Data comes from Envisat (top) descending track 079, dates 090201-090412 and (bottom) ascending track 129, dates 090311-090415, with the fault rupture modelled as a uniform dislocation in an elastic medium. The white line in the interferograms is the up-dip surface projection of our model fault plane. (modified from Walters et al., 2009).

The dataset encompasses a broad spectrum of earthquake kinematics (31 reverse, 23 normal, and 42 strike-slip events), depths (1–47 km), and magnitudes (M_w 3.9–9.0). Following Livio and Ferrario (2024), we adopt a log-linear formulation to relate the areal extent of deformation (A, in km^2) to M_w:

$$Log_{10}(A) = a(M_w) + b \quad (1)$$

where a and b are empirical coefficients. In this study, we recomputed these coefficients (Table 1) using the full Livio and Ferrario (2024) dataset, ensuring consistency with our methodological framework and allowing separate regressions for normal, reverse, and strike-slip events (Figure 2). Previous studies (Livio et al., 2017; Serva et al., 2019) reported that deformation area shows only a weak dependence on hypocentral depth, consistent with expectations for upper-crustal ruptures; therefore, depth was not included as a predictor. Similarly, the influence of kinematics on regression is limited, though we retain separate relations for each faulting style to respect their differing magnitude ranges and data distributions (Figure 2). Overall, M_w remains the dominant parameter controlling the spatial extent of surface deformation, providing a robust and physically meaningful basis for defining the deformation-based buffer used in this study. Moreover, the regressions show moderate to high coefficients of determination (R^2), consistent with previously published M_w–area relations. The standard deviation of the residuals reflects the natural variability of deformation footprints observed across different fault geometries, depths, and rupture complexities. These values indicate that M_w is the dominant predictor of deformed area, while the scatter is compatible with expectations from global InSAR-derived datasets.

3 Method for integrating on-fault and off-fault seismicity

To physically define the spatial domain where diffuse seismicity should be reduced, we derive the total deformation area associated with each active and capable fault from empirical M_w–deformed area relations (Eq. 1). For a given fault, this area represents the expected footprint of permanent ground deformation produced by earthquakes on that structure, as observed through global InSAR datasets. We then subtract the surface projection of the fault plane from this total area; the remaining portion defines a buffer region surrounding the fault, within which off-fault seismicity rates are progressively tapered (Figure 3). In the proposed approach, the contribution of off-fault seismicity is modified only in the vicinity of mapped active and capable faults. Regions located outside the deformation footprint of each fault are fully described by the original off-fault seismicity model, without any modification (Figure 3). This ensures that the model naturally incorporates unknown, unmapped, or secondary faults that are not included in the fault source model.

Each point of the off-fault seismicity model is assigned a distance d from the nearest point of the fault's plane surface projection (namely the Joyner-Boore distance). Points located outside the deformation-based

Kinematic	a	b	sD_{res}	R^2	M_w range	N
Normal	0.7469	-2.0284	0.2735	0.7469	3.9 – 7.1	23
Reverse	0.8754	-2.7524	0.3151	0.8656	4.9 – 9.0	31
Strike-slip	0.8854	-2.8401	0.3369	0.7907	4.4 – 7.8	42
All	0.8641	-2.7020	0.3184	0.8243	3.9 – 9.0	96

Table 1 Empirical regression coefficients for Eq. 1 for each kinematic class and for the full dataset. For each category (normal, reverse, strike-slip, and all events combined), the table reports the slope (a) and intercept (b), the coefficient of determination (R^2), the standard deviation of the residuals (sD_{res}), the number of events included in the regression (N), and the magnitude range over which the relation is applicable. The regressions are based on the updated InSAR-derived deformation dataset of Livio and Ferrario (2024), and the coefficients computed here are those used in this study to define the deformation-based buffer around each fault source.

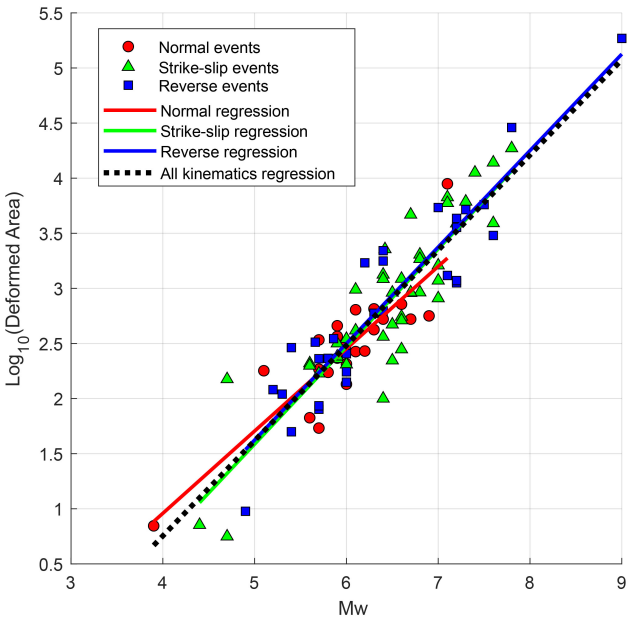

Figure 2 Empirical relation between M_w and deformed area derived from InSAR observations. Scatter plot of the 96 earthquakes compiled by Livio and Ferrario (2024), showing the log_{10}-transformed deformed area (km^2) as a function of moment magnitude, M_w. Events are grouped by faulting style: normal (red circles), strike-slip (green triangles), and reverse (blue squares). Solid lines represent the separate log-linear regressions for each kinematic class, while the dashed black line shows the regression obtained using all events regardless of mechanism.

buffer retain their original rates (Figure 3). Points located inside the fault plane projection have their rates for magnitudes $M_w > M_{min}$ removed entirely, in order to avoid double counting events that are already modelled as fault-based ruptures. In this case, M_{min} is the minimum magnitude of the seismogenic source. For points located within the deformation-based buffer, but outside the fault plane projection, the rates for magnitudes $M_w > M_{min}$ are reduced according to a distance-dependent weighting function:

$$w = \left(\frac{d}{D_{buffer}} \right)^p \tag{2}$$

where D_{buffer} is the buffer width (Figure 3) and p is an exponent controlling the smoothness of the taper (with $p = 1$ corresponding to a linear decay and $p > 1$ producing a steeper reduction near the fault). The final tapered rate (λ_t) for each magnitude bin M and for $M_w > M_{min}$ is given by:

$$\lambda_t(M) = w\lambda(M) \tag{3}$$

A power-law taper was selected because it provides a flexible and physically meaningful decay of off-fault seismicity rates near faults. Compared to a linear taper, the power-law formulation allows a steeper reduction of rates in the vicinity of the fault plane where large off-fault earthquakes are least likely, while still ensuring a smooth and gradual transition toward the outer edge of the deformation buffer. This behavior is consistent with observations from numerical and analogue models of fault system evolution, which show that the probability of hosting large independent ruptures decreases rapidly near major fault cores and increases only at larger distances. The power-law function therefore captures this non-linear gradient of deformation influence more realistically than the linear alternative, while avoiding the need for additional parameters required by exponential tapers. Its use also aligns with other recent ERF models (e.g., UCERF3 and the New Zealand National Seismic Hazard Model), facilitating methodological consistency while retaining transparency and reproducibility.

This formulation ensures that (1) off-fault seismicity is removed where ruptures are known to occur on the main seismogenic structure, (2) large-magnitude off-fault events become increasingly unlikely as the seismogenic structure is approached, and (3) the original distributed seismicity model is preserved far from faults. The resulting model provides a physically based and spatially smooth transition between on-fault and off-fault sources, relaxing the traditional dichotomy between the two and avoiding double counting in the overlapping magnitude range. Moreover, the spatial tapering modifies the off-fault seismicity only for magnitudes equal to or greater than the seismogenic source M_{min} and does not introduce any tapering of the regional maximum magnitude of the off-fault seismicity model. The regional maximum magnitude of the off-fault component is preserved for grid points located both outside and within the buffer, whereas within the fault plane projection the effective maximum magnitude is controlled exclusively by the seismogenic source.

For faults characterized by curved, segmented, or branched surface traces, the deformation-based buffer is constructed by following the mapped geometry of

each individual fault segment, rather than assuming a single straight fault trace or a uniform buffer geometry. The buffer width is defined consistently from the expected deformed area, but its spatial implementation is controlled locally by the fault geometry.

In regions where the deformation-based buffers of two or more nearby faults or fault segments overlap, a point of the diffuse seismicity model may fall within the buffer of multiple sources. In such cases, the reduction of rates is applied independently for each overlapping buffer. Specifically, the tapering weight associated with each fault is computed separately, and the final weight is obtained as the product of all applicable weights. This results in a stronger reduction where the influence zones of multiple major faults intersect, reflecting the reduced likelihood that large off-fault earthquakes occur in areas structurally dominated by more than one mapped seismogenic source. This multiplicative formulation preserves consistency with the physical interpretation of the buffer as a region influenced by fault-related deformation, and naturally accommodates complex, multi-fault environments.

4 Application example

To illustrate the practical implementation of the proposed approach, we applied the method to an active and capable fault and its surrounding off-fault seismicity grid. We apply the proposed method to the Paganica Fault, responsible for the 2009 L'Aquila (M_w 6.3) earthquake (e.g., Walters et al., 2009). The coseismic deformation mapped by InSAR for this event is shown in Figure 1. The fault geometry is taken from Valentini (2020): the fault length is 20 km, the source dips 50° and spans a 14 km seismogenic thickness. This geometry yields a fault plane surface projection of about 240 km^2. For a M_w of 6.5 (as inferred in Valentini, 2020), the characteristic magnitude of the source, the empirical relation presented in Eq. 1 predicts an expected total deformed area of approximately 670 km^2. By subtracting the 240 km^2 fault plane-projection area from the predicted total deformation, roughly 430 km^2 remain to be distributed around the seismogenic source. Assuming this residual area is uniformly spread around the fault plane surface projection (Figure 3), the corresponding deformation-based buffer width (D_{buffer}) is 5.1 km. The resulting deformation footprint is asymmetric (Figure 3), with a larger hanging-wall contribution, consistent with the typical InSAR-observed deformation patterns of dip-slip normal-faulting earthquakes (Figure 1).

Given that the maximum magnitude of the Paganica source is M_w 6.5 ± 0.2, the tapering of off-fault seismicity begins at M_w 6.3 (namely, M_{min}). For a buffer width of 5.1 km, a point located 1 km from the fault surface would receive a taper factor of w = 0.20 for a linear decay (p = 1), and w = 0.04 for a steeper power-law decay (p = 2). A point located 4.1 km from the fault would have w = 0.80 (p = 1) or w = 0.64 (p = 2). The resulting modified magnitude–frequency distributions for representative off-fault seismicity grid points are shown in Figure 4. Diffuse seismicity rates were computed using a smoothed kernel approach and a Gutenberg-Richter distribution following Valentini et al. (2017).

Figure 4 shows the three characteristic behaviors of the tapering function. For a point located outside the deformation-based buffer, the MFD remains identical to the original diffuse seismicity input. Points located within the buffer exhibit progressively reduced rates for magnitudes exceeding the seismogenic source M_{min}, with stronger reductions occurring closer to the fault plane projection (e.g., at a distance of d = 1 km). The exponent p controls the smoothness of the taper, with $p = 1$ corresponding to a linear decay and $p = 2$ producing a steeper reduction near the seismogenic source (Figure 4). Grid points falling within the surface projection of the fault plane have the rates for magnitudes above the seismogenic source M_{min} fully removed to avoid double counting. This portion of the MFD is instead accounted for by the activity rates assigned to the seismogenic source, whose maximum magnitude defines the upper bound of the combined MFD at these locations.

This simple example demonstrates that the deformation-based buffer produces a smooth and physically interpretable transition between fault and off-fault activity. It naturally removes supraseismogenic distributed events near major faults while preserving the original seismicity pattern away from mapped sources. The behaviour is stable across different source geometries and can accommodate multiple overlapping buffers by applying multiplicative weights.

5 Discussion

In PSHA, the explicit treatment of uncertainties is a fundamental requirement, as modeling choices can significantly influence hazard estimates. The framework proposed in this study introduces a number of assumptions that should be interpreted as sources of epistemic uncertainty rather than aleatory variability. These include the representation of the deformation footprint around faults, the parameterization of the taper controlling the reduction of off-fault seismicity rates, and the selection of empirical magnitude–area regressions under different tectonic conditions. Making these assumptions explicit allows them to be systematically explored through sensitivity analyses and logic-tree implementations.

In the proposed approach, the fault-plane surface projection is treated as an integral component of the total deformation footprint. Although the residual deformation area is geometrically distributed around the fault-plane projection using a uniform buffer for operational simplicity, the resulting deformation pattern is not necessarily symmetric when referenced to the surface fault trace (Figure 3). For dipping faults, the surface projection of the fault plane naturally extends preferentially toward the hanging wall, leading to deformation footprints that are consistent with InSAR observations of dip-slip earthquakes, where hanging-wall deformation typically dominates over the footwall. This behavior is clearly illustrated in the application example presented in Section 4 and indicates that, even under a geometrically simple buffering assumption, first-order deformation asymmetry is already implicitly cap-

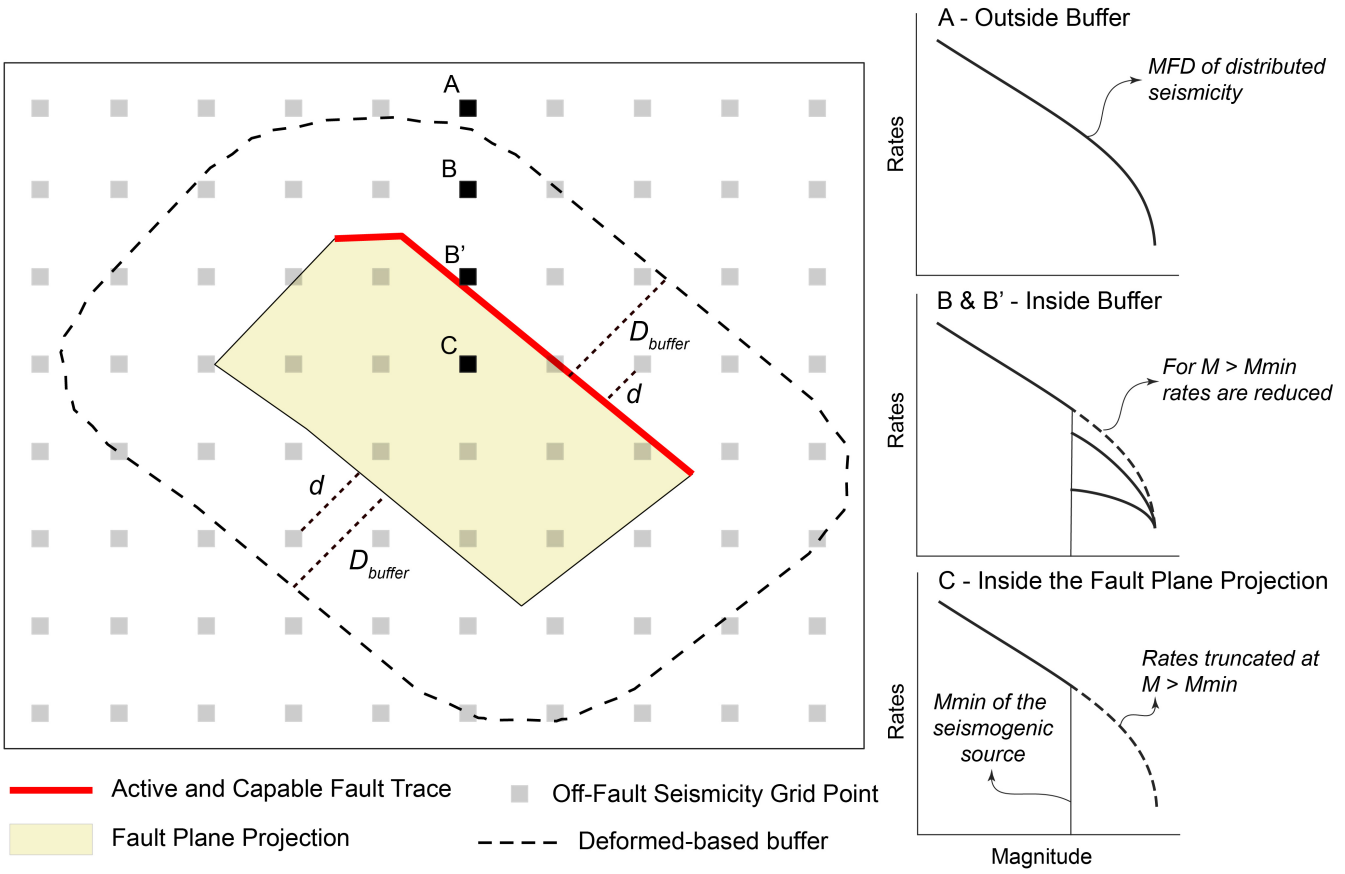

Figure 3 Schematic representation of the deformation-based buffer approach for tapering off-fault seismicity near a fault. The yellow polygon represents the surface projection of the fault, and the dashed line outlines the deformation-based buffer derived from (Eq. 1). Grey squares represent the diffuse seismicity grid points. Point A lies outside the buffer and retains the original rates. Points B and B' fall inside the buffer, and their rates for $M > M_{min}$ are reduced proportionally to their Joyner-Boore distance. Point C lies within the fault projection and its rates for $M > M_{min}$ are removed entirely. Right panels illustrate the expected modifications to the magnitude–frequency distributions for each case.

tured by the fault geometry. Future developments of the method could further refine this aspect by incorporating InSAR-derived statistics on hanging-wall and footwall deformation, enabling the construction of directionally dependent deformation buffers while preserving the overall simplicity and transparency of the framework.

Another key modeling choice concerns the taper exponent p, which controls the smoothness of the transition between fault-based and off-fault seismicity rates within the deformation buffer. A value of $p = 1$ corresponds to a linear decay, whereas values $p > 1$ produce a progressively steeper reduction of off-fault seismicity rates in the immediate vicinity of the fault and a smoother transition toward the outer edge of the buffer (Figure 4). Increasing p therefore enhances the suppression of diffuse seismicity near major seismogenic structures, where large independent off-fault earthquakes are least likely, while maintaining nonzero rates at larger distances. In this framework, p is treated as a tunable parameter whose optimal value depends on the tectonic setting and the objectives of the ERF model. Based on empirical considerations and practical testing, values in the range $1 \leq p \leq 2$ are recommended, with sensitivity analyses encouraged to evaluate their impact on the resulting hazard estimates.

The applicability of the method to complex tectonic environments also warrants consideration. In regions characterized by mixed or transitional fault kinematics, such as transpressional or transtensional regimes, the attribution of a single faulting style may be uncertain or spatially variable. In such cases, the empirical regression derived from the full dataset, independent of faulting style, provides a robust and operational alternative for estimating the expected deformation area. While style-specific regressions may be preferred where reliable kinematic information is available, the use of an all-kinematics relation ensures consistency and applicability in structurally complex regions. The choice of the regression model directly influences the predicted deformation area and, consequently, the width of the deformation-based buffer and the resulting modification of diffuse seismicity rates and should therefore be regarded as an explicit and testable modeling assumption.

In the proposed framework, the total deformation area is controlled exclusively by earthquake magnitude through the empirical magnitude–area relation,

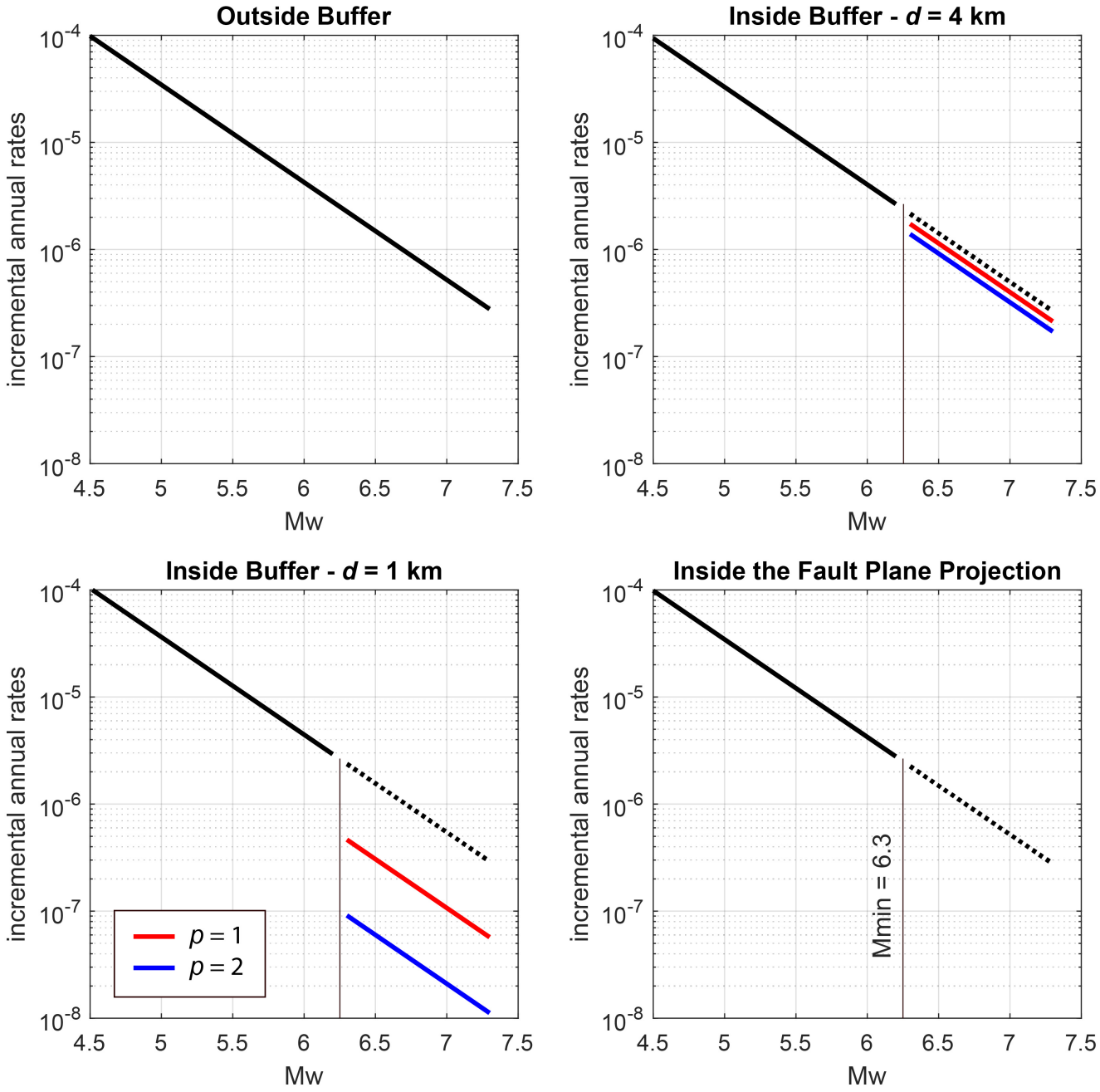

Figure 4 Incremental annual rates for four points of the grid where the off-fault seismicity has been calculated. Points lying outside the buffer retained their original rates, while points located inside the buffer experienced a distance-dependent reduction controlled by the power-law taper (p = 1 red lines and p = 2 blue lines). Rates for all magnitudes above the minimum magnitude (M_{min}) of the seismogenic source were removed entirely for points falling directly within the projected fault polygon.

whereas the geometry of the fault-plane surface projection governs how this area is partitioned between the fault projection itself and the surrounding deformation buffer. As a result, seismogenic depth and fault dip influence the buffer definition indirectly. Larger seismogenic thicknesses and lower dip angles increase the surface projection of the fault plane, thereby reducing the residual area assigned to the buffer, while preserving the same magnitude-dependent total deformation footprint. Conversely, near-vertical faults produce negligible surface projections, in which case the deformation footprint is represented almost entirely by the buffer. Moreover, the method is primarily intended for faults capable of rupturing the surface; although it can be applied to blind or deep-seated faults, caution is required, as surface deformation inferred from InSAR may be less representative of rupture dimensions, potentially leading to an overestimation of the effective deformation area. In this case, the buffer definition should be treated as a conservative upper bound.

Overall, the proposed framework is intentionally designed to make key modeling assumptions explicit and transparent. By treating parameters such as the taper exponent, deformation footprint geometry, and empir-

ical magnitude–area regression as sources of epistemic uncertainty, the method naturally lends itself to implementation within a PSHA logic-tree structure. This flexibility allows users to explore alternative representations of on-fault and off-fault seismicity and to assess their influence on seismic hazard estimates, supporting robust and defensible hazard analyses in both regional-scale and site-specific applications.

6 Conclusions

We introduced a physically motivated method for integrating fault-based and diffuse seismicity within earthquake rupture forecasts by leveraging an empirical relation between moment magnitude and the areal extent of permanent ground deformation. The deformation footprint provides a natural spatial domain over which off-fault seismicity should decrease, relaxing the traditional separation between on-fault and off-fault events. This transition is achieved through a distance-dependent power-law taper, which steepens near the fault surface—where independent large off-fault ruptures are unlikely—while remaining smooth and conservative at greater distances.

The method addresses two persistent challenges in combined ERF models: the potential double counting of earthquakes in the overlapping magnitude range and the artificial boundary between fault and distributed sources. By removing or reducing off-fault rates only within the deformation-derived buffer, the model ensures consistency with the physical dimensions of seismogenic structures and avoids abrupt or arbitrary spatial discontinuities.

A key advantage of the approach is its simplicity and adaptability. It can be implemented within any ERF framework, including those used in national seismic hazard models, without requiring complex tuning or extensive new datasets. The method also naturally incorporates regions where multiple deformation footprints overlap, further reducing the likelihood of supraseismogenic off-fault ruptures in structurally dominated areas. Overall, this deformation-based taper represents a transparent, reproducible, and physically informed solution that can improve the integration of fault and distributed seismicity in seismic hazard assessment.

Acknowledgements

This work was carried out within the framework of the Austrian Science Fund (FWF) project NEXTQUAKE (Project no.: PAT 2160424, Grant-DOI: 10.55776/PAT2160424). The author gratefully acknowledges the support of the FWF. No other specific funding was received for this study. The author also sincerely thanks the Associate Editor and the two reviewers, Francesco Visini and Aybars Gürpinar, for their careful reading of the manuscript and for their constructive and insightful comments, which significantly helped to improve the clarity and robustness of the paper.

7 Data and code availability

The InSAR-based deformation dataset used in this study is publicly available on Zenodo as published by Livio and Ferrario (2024). The empirical regression coefficients derived from this dataset and used in Eq. 1 are fully reported within the text. No additional datasets or code were generated for this study. All other information necessary to reproduce the method is provided in the manuscript.

8 Competing interests

The author declares that there are no competing interests.

References

Cornell, C. A. Engineering seismic risk analysis. *Bulletin of the Seismological Society of America*, 58(5):1583–1606, Oct. 1968. doi: 10.1785/bssa0580051583.

Cowie, P. A., Vanneste, C., and Sornette, D. Statistical physics model for the spatiotemporal evolution of faults. *Journal of Geophysical Research: Solid Earth*, 98(B12):21809–21821, Dec. 1993. doi: 10.1029/93jb02223.

Field, E. H., Arrowsmith, R. J., Biasi, G. P., Bird, P., Dawson, T. E., Felzer, K. R., Jackson, D. D., Johnson, K. M., Jordan, T. H., Madden, C., Michael, A. J., Milner, K. R., Page, M. T., Parsons, T., Powers, P. M., Shaw, B. E., Thatcher, W. R., Weldon, R. J., and Zeng, Y. Uniform California Earthquake Rupture Forecast, Version 3 (UCERF3)–The Time-Independent Model. *Bulletin of the Seismological Society of America*, 104(3):1122–1180, June 2014. doi: 10.1785/0120130164.

Gerstenberger, M. C., Bora, S., Bradley, B. A., DiCaprio, C., Kaiser, A., Manea, E. F., Nicol, A., Rollins, C., Stirling, M. W., Thingbaijam, K. K. S., Van Dissen, R. J., Abbott, E. R., Atkinson, G. M., Chamberlain, C., Christophersen, A., Clark, K., Coffey, G. L., de la Torre, C. A., Ellis, S. M., Fraser, J., Graham, K., Griffin, J., Hamling, I. J., Hill, M. P., Howell, A., Hulsey, A., Hutchinson, J., Iturrieta, P., Johnson, K. M., Jurgens, V. O., Kirkman, R., Langridge, R. M., Lee, R. L., Litchfield, N. J., Maurer, J., Milner, K. R., Rastin, S., Rattenbury, M. S., Rhoades, D. A., Ristau, J., Schorlemmer, D., Seebeck, H., Shaw, B. E., Stafford, P. J., Stolte, A. C., Townend, J., Villamor, P., Wallace, L. M., Weatherill, G., Williams, C. A., and Wotherspoon, L. M. The 2022 Aotearoa New Zealand National Seismic Hazard Model: Process, Overview, and Results. *Bulletin of the Seismological Society of America*, 114(1):7–36, Dec. 2023. doi: 10.1785/0120230182.

Gómez-Novell, O., Chartier, T., García-Mayordomo, J., Ortuño, M., Masana, E., Insua-Arévalo, J. M., and Scotti, O. Modelling earthquake rupture rates in fault systems for seismic hazard assessment: The Eastern Betics Shear Zone. *Engineering Geology*, 265: 105452, Feb. 2020. doi: 10.1016/j.enggeo.2019.105452.

Gürpinar, A., Serva, L., Livio, F., and Rizzo, P. C. Earthquake-induced crustal deformation and consequences for fault displacement hazard analysis of nuclear power plants. *Nuclear Engineering and Design*, 311:69–85, Jan. 2017. doi: 10.1016/j.nucengdes.2016.11.007.

International Atomic Energy Agency. The Contribution of Palaeoseismology to Seismic Hazard Assessment in Site Evaluation for Nuclear Installations. *TECDOC Series 1767, IAEA*, 2015.

International Atomic Energy Agency. Seismic hazards in site evaluation for nuclear installations, Specific Safety Guides SSG-9. *International Atomic Energy Agency*, 2022.

Leonard, M. Earthquake Fault Scaling: Self-Consistent Relating of Rupture Length, Width, Average Displacement, and Moment Release. *Bulletin of the Seismological Society of America*, 100(5A): 1971–1988, Sept. 2010. doi: 10.1785/0120090189.

Livio, F. and Ferrario, M. F. Empirical relation among earthquake magnitude (Mw) and deformed area as imaged by InSAR [Dataset], 2024. doi: 10.5281/ZENODO.11030647.

Livio, F., Serva, L., and Gürpinar, A. Locating distributed faulting: Contributions from InSAR imaging to Probabilistic Fault Displacement Hazard Analysis (PFDHA). *Quaternary International*, 451:223–233, Sept. 2017. doi: 10.1016/j.quaint.2016.09.034.

McGuire, R. K. Probabilistic seismic hazard analysis and design earthquakes: Closing the loop. *Bulletin of the Seismological Society of America*, 85(5):1275–1284, Oct. 1995. doi: 10.1785/bssa0850051275.

Meletti, C., Marzocchi, W., D'Amico, V., Lanzano, G., Luzi, L., Martinelli, F., Pace, B., Rovida, A., Taroni, M., Visini, F., Akinci, A., MPS Working Group: Anzidei, M., Avallone, A., Azzaro, R., Barani, S., Barberi, G., Barreca, G., Basili, R., Bird, P., Bonini, M., Burrato, P., Busetti, M., Camassi, R., Carafa, M. M. C., Cavaliere, A., Cecere, G., Cheloni, D., Chioccarelli, E., Console, R., Corti, G., D'Agostino, N., Dal Cin, M., D'Ambrosio, C., D'Amico, M., D'Amico, S., Devoti, R., Esposito, A., Faenza, L., Falcone, G., Felicetta, C., Fracassi, U., Franco, L., Galvani, A., Gasperini, P., Gee, R., Gomez Capera, A. A., Iervolino, I., Kastelic, V., Lai, C. G., Locati, M., Lolli, B., Maesano, F. E., Marchesini, A., Mariucci, M. T., Martelli, L., Massa, M., Metois, M., Monaco, C., Montone, P., Moschetti, M., Murru, M., Pacor, F., Pagani, M., Pasolini, C., Peresan, A., Peruzza, L., Pietrantonio, G., Poli, M. E., Pondrelli, S., Puglia, R., Rebez, A., Riguzzi, F., Roselli, P., Rotondi, R., Russo, E., Sani, F., Santulin, M., Selvaggi, G., Scafidi, D., Selva, J., Sepe, V., Serpelloni, E., Slejko, D., Spallarossa, D., Stallone, A., Tamaro, A., Tarabusi, G., Tiberti, M. M., Tuvè, T., Valensise, G., Vallone, R., Vannoli, P., Vannucci, G., Varini, E., Zanferrari, A., and Zuccolo, E. The new Italian seismic hazard model (MPS19). *Annals of Geophysics*, 64(1): SE112, Mar. 2021. doi: 10.4401/ag-8579.

Petersen, M. D., Shumway, A. M., Powers, P. M., Field, E. H., Moschetti, M. P., Jaiswal, K. S., Milner, K. R., Rezaeian, S., Frankel, A. D., Llenos, A. L., Michael, A. J., Altekruse, J. M., Ahdi, S. K., Withers, K. B., Mueller, C. S., Zeng, Y., Chase, R. E., Salditch, L. M., Luco, N., Rukstales, K. S., Herrick, J. A., Girot, D. L., Aagaard, B. T., Bender, A. M., Blanpied, M. L., Briggs, R. W., Boyd, O. S., Clayton, B. S., DuRoss, C. B., Evans, E. L., Haeussler, P. J., Hatem, A. E., Haynie, K. L., Hearn, E. H., Johnson, K. M., Kortum, Z. A., Kwong, N. S., Makdisi, A. J., Mason, H. B., McNamara, D. E., McPhillips, D. F., Okubo, P. G., Page, M. T., Pollitz, F. F., Rubinstein, J. L., Shaw, B. E., Shen, Z., Shiro, B. R., Smith, J. A., Stephenson, W. J., Thompson, E. M., Thompson Jobe, J. A., Wirth, E. A., and Witter, R. C. The 2023 US 50-State National Seismic Hazard Model: Overview and implications. *Earthquake Spectra*, 40(1):5–88, Feb. 2024. doi: 10.1177/87552930231215428.

Serva, L., Livio, F. A., and Gürpinar, A. Surface Faulting and Ground Deformation: Considerations on Their Lower Detectable Limit and on FDHA for Nuclear Installations. *Earthquake Spectra*, 35 (4):1821–1843, Nov. 2019. doi: 10.1193/110718eqs253m.

Serva, L., Livio, F. A., Bonadeo, L., and Colombo, M. The use of the area deformed by earthquakes (deformed area method) for potential fault capability assessment. *Nuclear Engineering and Design*, 444:114380, Dec. 2025. doi: 10.1016/j.nucengdes.2025.114380.

Stirling, M., Verry, G., and Berryman, K. A New Seismic Hazard Model for New Zealand. *Bulletin of the Seismological Society of America*, 92(5):1878–1903, June 2002. doi: 10.1785/0120010156.

Stirling, M., McVerry, G., Gerstenberger, M., Litchfield, N., Van Dissen, R., Berryman, K., Barnes, P., Wallace, L., Villamor, P., Langridge, R., Lamarche, G., Nodder, S., Reyners, M., Bradley, B., Rhoades, D., Smith, W., Nicol, A., Pettinga, J., Clark, K., and Jacobs, K. National Seismic Hazard Model for New Zealand: 2010 Update. *Bulletin of the Seismological Society of America*, 102(4): 1514–1542, Aug. 2012. doi: 10.1785/0120110170.

Thingbaijam, K. K. S., Martin Mai, P., and Goda, K. New Empirical Earthquake Source-Scaling Laws. *Bulletin of the Seismological Society of America*, 107(5):2225–2246, Sept. 2017. doi: 10.1785/0120170017.

Valentini, A. Allowing multi-fault earthquakes and relaxing fault segmentation in Central Apennines (Italy): Hints for fault-based PSHA. *Bulletin of Geophysics and Oceanography*, 62(4):647–688, 2020. doi: 10.4430/bgta0339.

Valentini, A., Visini, F., and Pace, B. Integrating faults and past earthquakes into a probabilistic seismic hazard model for peninsular Italy. *Natural Hazards and Earth System Sciences*, 17 (11):2017–2039, Nov. 2017. doi: 10.5194/nhess-17-2017-2017.

Walters, R. J., Elliott, J. R., D'Agostino, N., England, P. C., Hunstad, I., Jackson, J. A., Parsons, B., Phillips, R. J., and Roberts, G. The 2009 L'Aquila earthquake (central Italy): A source mechanism and implications for seismic hazard. *Geophysical Research Letters*, 36(17), Sept. 2009. doi: 10.1029/2009gl039337.

Wells, D. L. and Coppersmith, K. J. New empirical relationships among magnitude, rupture length, rupture width, rupture area, and surface displacement. *Bulletin of the Seismological Society of America*, 84(4):974–1002, Aug. 1994. doi: 10.1785/bssa0840040974.